1   **Title**

2   An Age-Specific Atlas for Delineation of White Matter Pathways in Children

3   Aged 6-8 Years

4   **Author names and affiliations**

5   Arthur Spencer[a]*, Hollie Byrne[a], Richard Lee-Kelland[b], Sally Jary[b], Marianne Thoresen[b,c], Frances

6   Cowan[b,d], Ela Chakkarapani[b], Jonathan C.W. Brooks[a,e].

7   [a]Clinical Research and Imaging Centre, University of Bristol, Bristol, UK

8   [b]Faculty of Health Sciences, Translational Health Sciences, Bristol Medical School, University of

9   Bristol, Bristol, UK

10   [c]Faculty of Medicine, Institute of Basic Medical Sciences, University of Oslo, Oslo, Norway

11   [d]Department of Paediatrics, Imperial College London, London, UK

12   [e]School of Psychological Science, University of Bristol, Bristol, UK

13   *Corresponding author; arthur.spencer@bristol.ac.uk; Clinical Research and Imaging Centre,

14   University of Bristol, 60 St Michael´s Hill, Bristol, BS2 8DX

15   **Declarations of interest:** none

16   **CRediT authorship contribution statement:**

17   Arthur Spencer: Conceptualisation; data curation; formal analysis; methodology; software; validation;

18   visualisation; writing – original draft.

19   Hollie Byrne: Data curation; investigation.

20   Richard Lee-Kelland: Data curation; investigation.

21   Sally Jary: Investigation.

22   Marianne Thoresen: Investigation.

23   Frances Cowan: Investigation.

24   Ela Chakkarapani: Funding acquisition; methodology; project administration; resources; supervision;

25   validation; writing – review & editing.

26   Jonathan Brooks: Methodology; resources; supervision; validation; writing – review & editing.

Abstract

Diffusion MRI allows non-invasive assessment of white matter maturation in typical development and of white matter damage due to brain injury or pathology. Reliably attributing diffusion metrics to specific white matter pathways either requires use of lengthy acquisition protocols with numerous diffusion directions, which may be problematic in certain cohorts (e.g. children or adults with mild cognitive impairment), or probabilistic white matter atlases, which allow delineation of white matter tracts without the need to perform tractography, thus eliminating the need for the extensive scans required for modern tractography algorithms. However, given the known age-dependency of developmental change in white matter it may not be optimal to use an adult template when assessing data acquired from children.

This study develops an age-specific probabilistic white matter atlas for delineation of 12 major white matter tracts in children aged 6-8 years. By comparing to fibre tracking in individuals, we demonstrate that this age-specific atlas gives better overall performance than simply registering to the Johns Hopkins University (JHU) adult white matter template in both data acquired from a single cohort on a single scanner (age-specific $r = 0.72$; JHU $r = 0.54$) and from a cohort taken from the ABIDE dataset (age-specific $r = 0.75$; JHU $r = 0.72$). Accuracy was assessed by comparing estimates of tract-level diffusion metrics, using the age-specific and adult templates, to results of subject-specific tracing. To our knowledge, this is the first publicly available probabilistic atlas of white matter tracts for this age group.

We then use the age-specific atlas to provide evidence for reduced fractional anisotropy in several tracts in children who were treated with therapeutic hypothermia for neonatal encephalopathy at birth and did not have cerebral palsy, compared with controls matched for age, sex and socio-economic status.

Keywords

White matter, Development, Atlas, dMRI, Tractography.

Abbreviations

DWI – diffusion-weighted imaging; FA – fractional anisotropy; NE – neonatal encephalopathy; TH – therapeutic hypothermia.

1 Introduction

Tract-level analysis of diffusion weighted imaging (DWI) data is used extensively to investigate white matter microstructure in both typical (Asato et al., 2010; Hüppi and Dubois, 2006; Lebel et al., 2008) and atypical brain development (for a review, see (Dennis and Thompson, 2013)). In children and adolescents, atypical brain development may lead to physical and intellectual disabilities including e.g. cerebral palsy (CP) (Arrigoni et al., 2016), autistic spectrum behaviours (Ameis and Catani, 2015; Dimond et al., 2019) and attention deficit hyperactivity disorder (Konrad and Eickhoff, 2010).

A widely employed technique to delineate white matter tracts is to segment streamlines generated by tractography (Lawes et al., 2008; Sydnor et al., 2018; Wakana et al., 2007; Wassermann et al., 2010; Zhang et al., 2018), however acquiring accurate tractography requires lengthy scanning protocols (i.e. HARDI) which are susceptible to head motion. Extended scan times can be problematic for some children, especially those with disabilities who would benefit from investigating white matter development (Phan et al., 2018).

Where long scans pose difficulty, shorter sequences can still provide the data required to construct diffusion tensors. Though not optimal, the tensor model offers insight into white matter microstructure by calculating metrics such as fractional anisotropy (FA), mean diffusivity (MD), radial diffusivity (RD) and axial diffusivity (AD) (Assaf and Pasternak, 2008). These metrics are sensitive to changes in the underlying white matter structure, thus are widely investigated in brain development (Dennis and Thompson, 2013; Lebel et al., 2008), as well as having clinical relevance in patient cohorts (Assaf et al., 2019; Assaf and Pasternak, 2008; Horsfield and Jones, 2002). Lacking the high angular resolution data required for tractography, white matter tracts can be delineated by registering to a standard template with a probabilistic atlas of tract locations. However, the widely used Johns Hopkins University (JHU) atlas (Hua et al., 2008) is constructed from adult data. Numerous developmental studies demonstrate white matter alterations continuing into adolescence (Cascio et al., 2007; Hagmann et al., 2010; Lebel et al., 2008; Simmonds et al., 2014), and white matter development varies widely across the brain (Lebel et al., 2019), therefore an atlas constructed from adult scans is by design and definition not representative of children. There are several publicly available age-specific structural templates (Altaye et al., 2008; Fonov et al., 2011; Richards et al., 2016; Sanchez et al., 2012), however none of these provide diffusion data.

Using robust tract reconstruction protocols (Wakana et al., 2007) this study develops an age-specific probabilistic white matter atlas for 12 major tracts in children aged 6-8 years. To assess whether this atlas accurately delineates tracts, we measured both volumetric overlap and the diffusion metrics sampled by the tract mask in comparison with tractography-based tract delineation. We then assess

88   the utility of this age-specific tract atlas by comparing it to results obtained using an adult atlas (JHU).

89   The atlas is then further validated against an open data source (i.e. different scanner), and against a

90   different tractography algorithm.

91   As a demonstration of proof of concept, we then investigate tract-level differences in children treated

92   with therapeutic hypothermia (TH) for neonatal encephalopathy (NE) at birth, compared with healthy

93   controls, and compare results obtained using the age-specific atlas to those from the JHU atlas. The

94   children who had TH, do not have CP and are in mainstream education still exhibit significantly

95   reduced performance on cognitive tests (Jary et al., 2019; Lee-Kelland et al., 2020) and have slower

96   reaction times and reduced visuo-spatial processing abilities (Tonks et al., 2019), compared to the

97   healthy controls.

98   This age-specific atlas provides a method of delineating white matter tracts in children without

99   tractography, thus lending itself to clinical settings, application to large datasets, and research studies

100   involving cohorts who may be averse to long scan times.

2 Material and Methods

2.1 Participants

103   Ethics approval was obtained from the North Bristol Research Ethics Committee and the Health

104   Research Authority (REC ID: 15/SW/0148). Informed and written consent was obtained from the

105   parents of participants before collecting data. The cohort was made up of 36 healthy children aged 6-8

106   years with no evidence of neurological disease, originally recruited as controls for a study of the long-

107   term effects of TH ("CoolMRI") on behavioural and imaging outcomes. The 36 controls were split

108   randomly into 28 atlas and 8 validation subjects such that the group were matched for age, sex, socio-

109   economic status (SES) and full-scale intelligence quotient (FSIQ). For the demonstrative case study,

110   data from 33 children treated with TH following NE at birth were compared to the control data.

111   Participant demographics are shown in Section 3.1.

2.2 Image Acquisition

113   DWI data were acquired with a Siemens 3 Tesla Magnetom Skyra MRI scanner at the Clinical

114   Research and Imaging Centre (CRiCBristol), Bristol, UK. Subjects were placed supine within the 32-

115   channel receive only head-coil by an experienced radiographer, and head movement minimised by

116   means of memory-foam padding. Children wore earplugs and were able to watch a film. A parent was

117   only allowed in the room in exceptional circumstances (i.e. if the child was very nervous). A

118   multiband echo-planar imaging (EPI) sequence was used with the following parameters: TE = 70 ms;

119   TR = 3150 ms; field of view 192 × 192 mm; 60 slices; 2.0 mm isotropic voxels; phase encoding in the

120   anterior-posterior direction, in-plane acceleration factor = 2 (GRAPPA (Griswold et al., 2002)),

121   through-plane multi-band factor = 2 (Moeller et al., 2010; Setsompop et al., 2012b, 2012a).

122   For the purpose of data averaging and eddy-current distortion correction, two sets of diffusion

123   weighted images were acquired with b = 1,000 s mm^{-2} in 60 diffusion directions, equally distributed

124   according to an electrostatic repulsion model, as well as 8 interspersed b = 0 images, with one data set

125   acquired with positive phase encoding steps, then repeated with negative steps (so-called, "blip-up",

126   "blip-down"), giving a total of 136 images.

2.3 Quality Control

128   The quality of the diffusion data was assessed using the EddyQC tool (Bastiani et al., 2019) from FSL

129   (Smith et al., 2004). This provides several measures of the amount of movement and eddy current

130   induced distortion present in the data. For each participant, the root-mean-square of all metrics was

131   calculated, giving a score which increases monotonically with the amount of movement and eddy

132   current distortion. Scans were rejected if their score was more than one standard deviation above the

133   mean of all participants.

## 2.4 Image Processing & Atlas Construction

135   DWI data were denoised and corrected for eddy current induced distortions and subject movements

136   using EDDY (Andersson and Sotiropoulos, 2016) and TOPUP (Andersson et al., 2003), part of FSL.

137   Subsequent DWI processing and tractography steps were performed using MRtrix (Tournier et al.,

138   2019). The response function (the DWI signal for a typical fibre population) was estimated from the

139   data (Tournier et al., 2013). The fibre orientation distribution (FOD) was then calculated by

140   performing constrained spherical deconvolution of the response function from the measured DWI

141   signal (Tournier et al., 2007). Deterministic tractography was run in each subject using the "SD

142   Stream" algorithm (Tournier et al., 2012). Streamlines were seeded randomly in the brain and

143   generated with a step size of 0.2 mm, then terminated if the FOD amplitude dropped below 0.2 or the

144   angle between successive steps exceeded 40 degrees. 10 million streamlines were generated, which

145   were then filtered to 1 million using spherical-deconvolution informed filtering of tractograms (SIFT)

146   (Smith et al., 2013) to give better reconstruction of FODs, improving anatomical accuracy.

147   The process of generating probability maps from the whole-brain tractograms is summarised in Figure

148   1. White matter tracts were segmented from whole-brain tractograms using the protocols described in

149   (Wakana et al., 2007), whereby regions of interest (ROI) are drawn to include or exclude streamlines

150   passing through them. For a given tract, any streamlines which pass through all inclusion ROIs and no

5

151 exclusion ROIs belong to that tract, and all other streamlines are removed. Inclusion and exclusion

152 ROIs were manually drawn in each subject to delineate 12 major fibre tracts: anterior thalamic

153 radiation (ATR); cingulate gyrus part of the cingulum (CG); hippocampal part of the cingulum (CH);

154 cortico-spinal tract (CST); forceps major (Fmajor); forceps minor (Fminor); inferior fronto-occipital

155 fasciculus (IFOF); inferior longitudinal fasciculus (ILF); superior longitudinal fasciculus (SLF);

156 temporal part of the superior longitudinal fasciculus (SLFt); uncinate fasciculus (UF); and the fornix.

157 The locations of ROIs for all tracts apart from the fornix are described in (Wakana et al., 2007), as

158 shown in Figure 2.

159
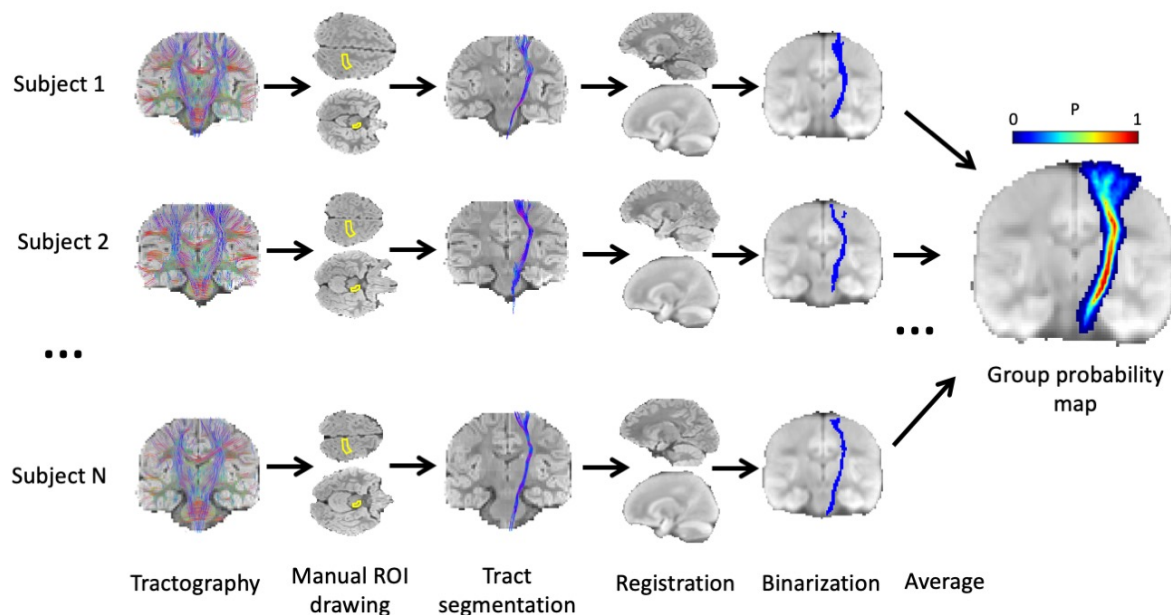
160 **Figure 1:** Methodology for generating probabilistic tract maps from whole-brain tractography data,

161 shown here for the corticospinal tract (CST). ROIs were manually drawn in each subject, as defined

162 by (Wakana et al., 2007) (in the case of the CST, inclusion ROIs were drawn in the cerebral peduncle

163 and the primary motor cortex), and tracts were segmented by including streamlines passing through

164 the inclusion ROIs. Streamlines were transformed to standard space (JHU template) and a binary

165 mask was created for each subject indicating all voxels containing streamlines. The average of these

166 masks (across N = 28 subjects) gives the probability map.
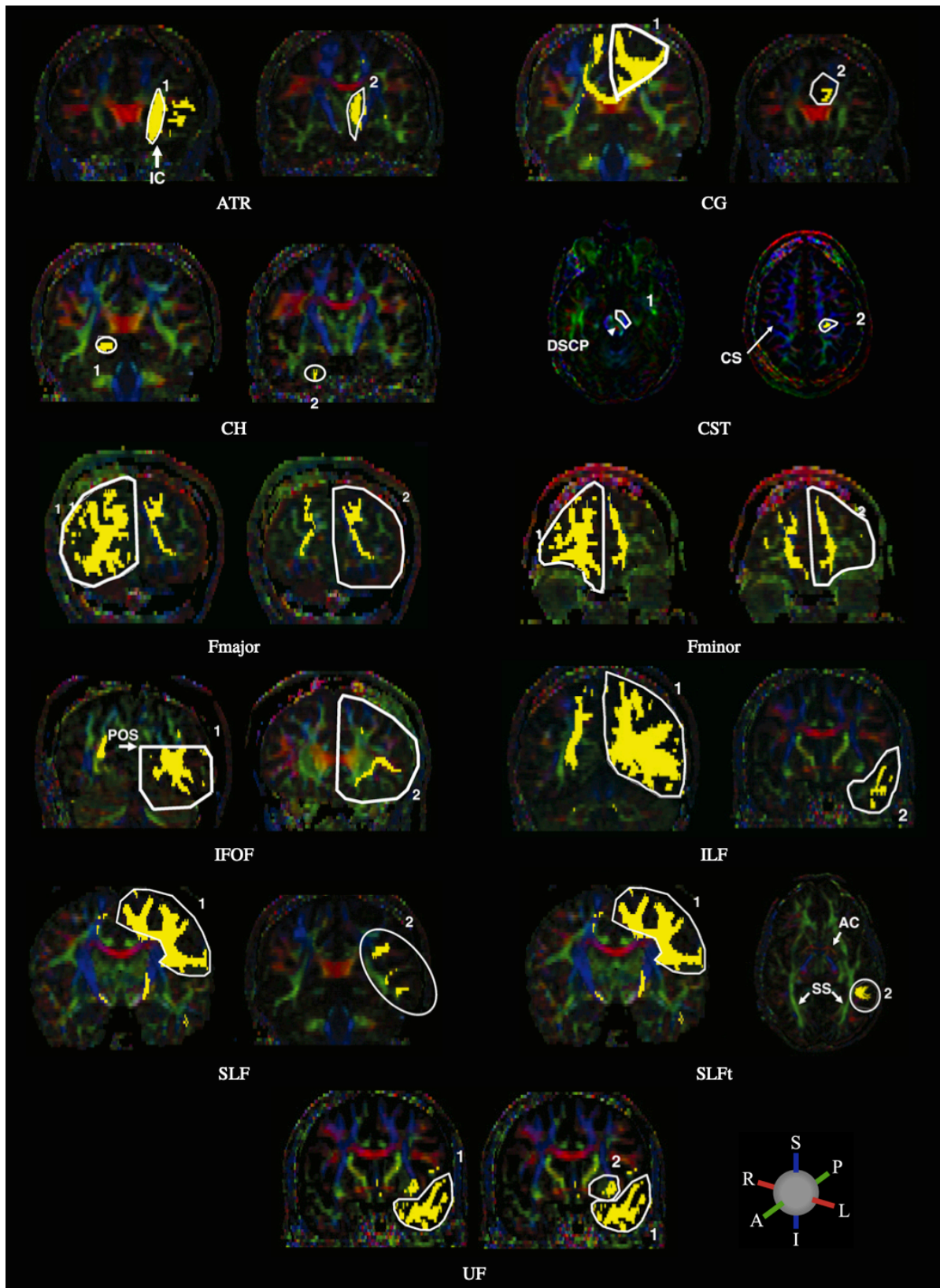
Figure 2: ROIs used to delineate the following major white matter tracts: anterior thalamic radiation (ATR); cingulate gyrus part of the cingulum (CG); hippocampal part of the cingulum (CH); cortico-spinal tract (CST); forceps major (Fmajor); forceps minor (Fminor); inferior fronto-occipital

7

171   fasciculus (IFOF); inferior longitudinal fasciculus (ILF); superior longitudinal fasciculus (SLF);

172   temporal part of the superior longitudinal fasciculus (SLFt); uncinate fasciculus (UF). Streamlines are

173   included in a given tract if they pass through both 1 AND 2. The following abbreviations indicate

174   anatomical landmarks used to draw the ROIs: internal capsule (IC); decussation of the superior

175   cerebellar peduncle (DSCP); central sulcus (CS); parieto-occipital sulcus (POS); anterior commissure

176   (AC); sagittal stratum (SS). ROIs are drawn in white with streamlines in yellow, overlaid on FA

177   images with principal diffusion directions indicated by the colour ball; blue = superior-inferior (S-I),

178   green = anterior-posterior (A-P) and red = right-left (L-R). Adapted from (Wakana et al., 2007) with

179   permission from Elsevier.

180   To delineate the fornix, streamlines were included which pass through the body of the fornix and

181   either of the posterior limbs which project to the hippocampus (Figure 3). These were isolated by first

182   selecting an axial level at the lower edge of the splenium of the corpus callosum, as seen in the mid-

183   sagittal plane (Figure 3, left); in this axial level, the first ROI was drawn around the body of the

184   fornix. Viewing the streamlines which are delineated by the first ROI, additional bilateral ROIs were

185   defined to include only those which project posteriorly from the fornix body (Figure 3, right).
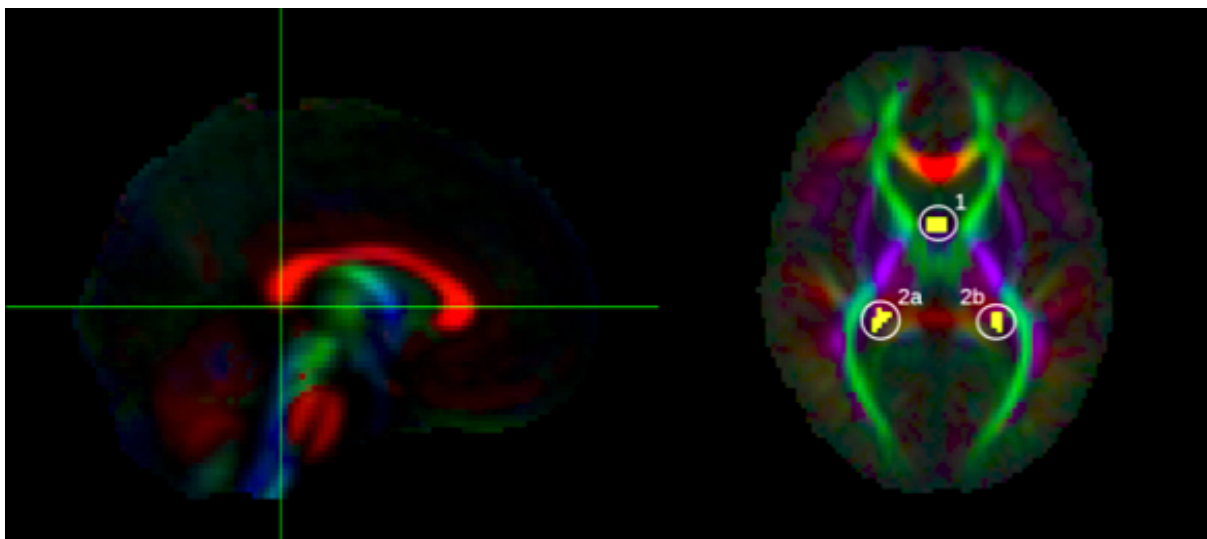
186

187   **Figure 3:** ROIs used to delineate the fornix, shown here on the group FA template. Yellow voxels

188   contain streamlines which pass through the body of the fornix (1) AND bilateral posterior limbs of

189   fornix (2a OR 2b).

190   For spatial normalisation, the average diffusion weighted image (aDWI), created for each subject by

191   averaging all DWI images, was registered to the JHU aDWI template by 12-degree of freedom affine

192   registration using FSL's FLIRT (Jenkinson et al., 2002). The resulting transformation was then

193   applied to the segmented streamlines. Any voxel containing one or more of these streamlines was then

194   labelled, to create a binary mask for the tract for each individual. The average, across 28 subjects, of

8

195 these binary masks was taken to give a probability map for each tract. The aDWI was then created for

196 the group by averaging transformed aDWIs from all 28 subjects, and the group FA image was created

197 from the group-average tensor map.

198 This atlas is available at Neurovault (https://neurovault.org/collections/LWTAAAST/)[1]. Data is

199 available upon request to the corresponding author.

2.5 Validation

201 Two datasets were used for validation. The first was made up of 8 subjects drawn randomly from the

202 36 control participants from CoolMRI. These subjects were scanned using the same scanner and

203 scanning parameters as the remaining 28 subjects used in construction of the atlas. Subject specific

204 tracts were traced in these individuals using the method described in Section 2.4.

205 The second validation dataset comprises data obtained from the Autism Brain Imaging Data

206 Exchange II[2] (ABIDE) database (Di Martino et al., 2017), available online as part of the International

207 Neuroimaging Data Sharing Initiative. This allows validation using subjects scanned in a different

208 scanner, and with different scanning parameters, in order to alleviate any bias associated with same-

209 site scans. Scans were obtained from 7 subjects, aged 8-9 years. Both typical controls (n = 3) and

210 subjects with autism spectrum disorder (n = 4) were used. Due to data availability the age range of

211 these subjects extends slightly above that of the atlas, however it serves as a test of how well the atlas

212 generalises. These images were acquired on a GE 3T MR750 scanner with an 8-channel head coil

213 using an echo-planar pulse sequence with the following parameters: TE = 84.9 ms; TR = 8500 ms;

214 FoV = 240 mm; 128 x 128 matrix; 68 slices; 1.88 x 1.88 x 2 mm resolution; 61 diffusion directions

215 with b = 1,000 s mm^{-2}; and one b = 0 image. To remove any further bias resulting from the validation

216 data being processed with the same tractography algorithm, tracts in the ABIDE subjects were traced

217 using a deterministic tensor-based algorithm (Basser et al., 2000).

218 After all tracts were traced in every validation subject, they were nonlinearly registered to the group

219 FA image, constructed from the 28 atlas subjects, using FSL's FNIRT (Andersson et al., 2007). To

220 compare spatial similarity between normalised data we tested the volumetric overlap between the

221 probabilistic atlas (age-specific or JHU) and each individually traced tract by measuring the Dice

222 score (Dice, 1945) over a range of thresholds. The amount of volumetric overlap between the atlas

223 data and the individually traced tract will depend on both i) the quality of registration of the individual

224 to the template, and ii) the agreement between the atlas data and the results from tractography in the

---

[1] Currently accessible only via this link. Repository will be made public upon publishing.
[2] http://fcon_1000.projects.nitrc.org/indi/abide/abide_II.html

225 individual. Thus, if the template is a closely matched target for registration, and if the underlying

226 anatomy and diffusion process captured by the atlas is a good match to the validation subjects, we

227 expect the Dice scores to be high.

228 We then assessed the ability of the atlas to reproduce individually traced DWI metrics by calculating

229 the mean FA in every slice along the major axis of each tract (coronal slices for tracts which project

230 anterior/posterior; axial slices for tracts which project dorsal/ventral). In individually traced tracts,

231 average FA was calculated by taking the mean FA in all masked voxels. In the probabilistic atlas, the

232 FA was weighted by the probability in each voxel using:

$$\text{FA} = \frac{\sum_i \text{FA}_i \times P_i}{\sum_i P_i} \tag{1}$$

233 where FA_i is the FA in voxel i and P_i is the probability in voxel i. The Pearson correlation coefficient

234 was then calculated between the probabilistic FA and individual FA. The average FA over the whole

235 tract was also calculated for both probabilistic and individual tracts. The correlation, over all tracts,

236 between probabilistic and individual measurements was assessed. Bland-Altman plots (Altman and

237 Bland, 1983) were also constructed to compare the precision and accuracy of whole-tract FA

238 measured by the atlas with individually traced measurements. The same methods were also applied to

239 the JHU atlas for comparison.

240 Whole-tract correlation plots and Bland-Altman plots were constructed for the 7 ABIDE subjects to

241 assess the generalisation of the age-specific atlas. This is a deliberately conservative test due to the

242 different age range and suboptimal tractography algorithm (see Section 4, Discussion). Validation of

243 the volumetric overlap and slice-wise correlations for the ABIDE subjects are also provided in the

244 supplementary materials for completeness.

2.6 Case Study

246 As a demonstration, the age-specific atlas produced here was used to investigate tract-level

247 differences in white matter microstructure between the case and control children of the CoolMRI

248 study. In all the tracts delineated by the age-specific atlas, the average FA in the tract was calculated

249 for each individual using Equation 1. Bilateral tracts were tested separately. Mann-Whitney U tests

250 were applied to test for differences in the median FA between cases and controls in each tract, with

251 Bonferroni correction applied to correct for family-wise error. Significant results have corrected p <

252 0.05. For comparison, the equivalent analysis was performed using the adult-derived JHU atlas. In the

253 absence of "ground-truth", only a qualitative comparison of results obtained with the two atlases was

254 performed.

10

3 Results

3.1 Participant Demographics

The CoolMRI study recruited 51 children, without CP, treated with TH for NE at birth and 43 control children matched for age, sex and SES (Lee-Kelland et al., 2020). Of the recruited children, 7 cases and 4 controls did not want to undergo scanning. A further 4 cases had incomplete data due to movement during the scan. Quality control (Section 2.3) led to the rejection of a further 6 cases and 2 controls. One further case and one control were rejected due to incorrect image volume placement. This left 33 cases and 36 controls. These controls were split into 28 (15 M) for atlas construction and 8 (4 M) for validation. Data for each set of participants is shown in Table 1.

	Atlas Data			TH Data		
	Atlas (n = 28)	Validation (n = 8)	p	Cases (n = 33)	Controls (n = 36)	p
Age	7.0 (6.1-7.9)	7.0 (6.1-7.8)	0.9392	6.9 (6.0-7.9)	7.0 (6.1-7.9)	0.5595
SES	B (A-D)	B (A-C1)	0.7305	C1 (A-E)	B (A-D)	0.1568
M/F	15/13	4/4	0.8776	18/15	19/17	0.8894
FSIQ	108 (75-127)	112.5 (88-137)	0.3032	93 (62-115)	108 (75-137)	<0.0001

Table 1: Demographics of participants in the atlas and validation dataset, and in the TH dataset. Mean (range) is shown for age; Median (range) is shown for SES and FSIQ. SES is defined as follows: A= upper middle class, B = middle class, C1 = lower middle class, C2 = skilled working class, D = working class.

3.2 Atlas

Figure 4 shows the probabilistic map for each tract, as well as the aDWI and FA images for the group of 28 children.

11
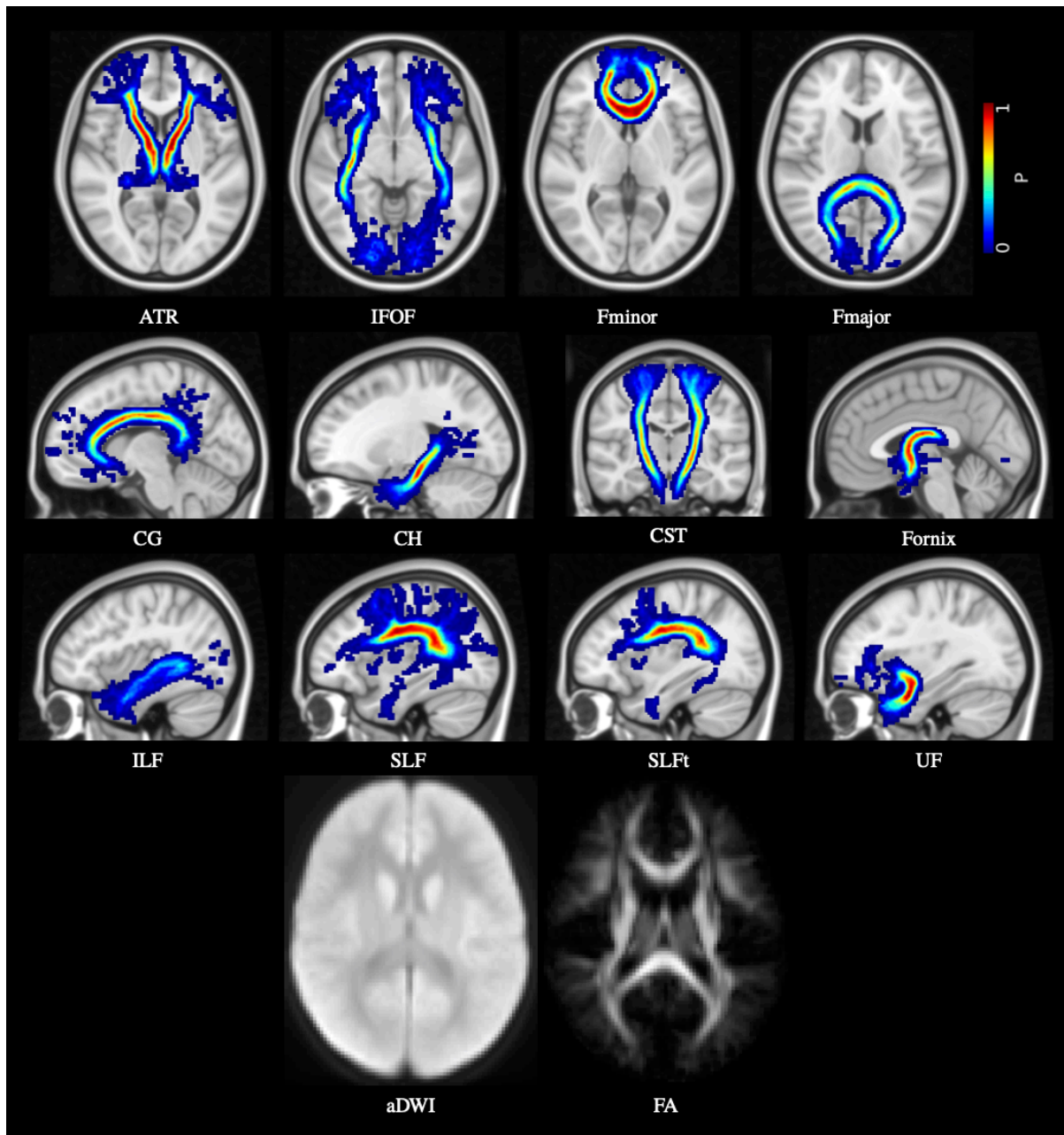
Figure 4: Age-specific probabilistic atlas for the 12 major white matter tracts: anterior thalamic radiation (ATR); inferior fronto-occipital fasciculus (IFOF); forceps minor (Fminor); forceps major (Fmajor); cingulate gyrus part of the cingulum (CG); hippocampal part of the cingulum (CH); cortico-spinal tract (CST); fornix; inferior longitudinal fasciculus (ILF); superior longitudinal fasciculus (SLF); temporal part of the superior longitudinal fasciculus (SLFt); and uncinate fasciculus (UF). Probabilities are indicated by the colour bar. Also shown are the aDWI and FA maps.

12

3.3 Validation

3.3.1 Volumetric Overlap

The Dice score at a range of thresholds is plotted for each tract for the same-site data in Figure 5, and the ABIDE data in Figure S1. In the same-site validation data, the peak of the median Dice score for the age-specific atlas is higher than for the JHU atlas in every tract. In the ABIDE data, though the difference is smaller, the peak of the median Dice score for the age-specific atlas is higher than for the JHU atlas in all tracts apart from the Fmajor and CST and SLF.
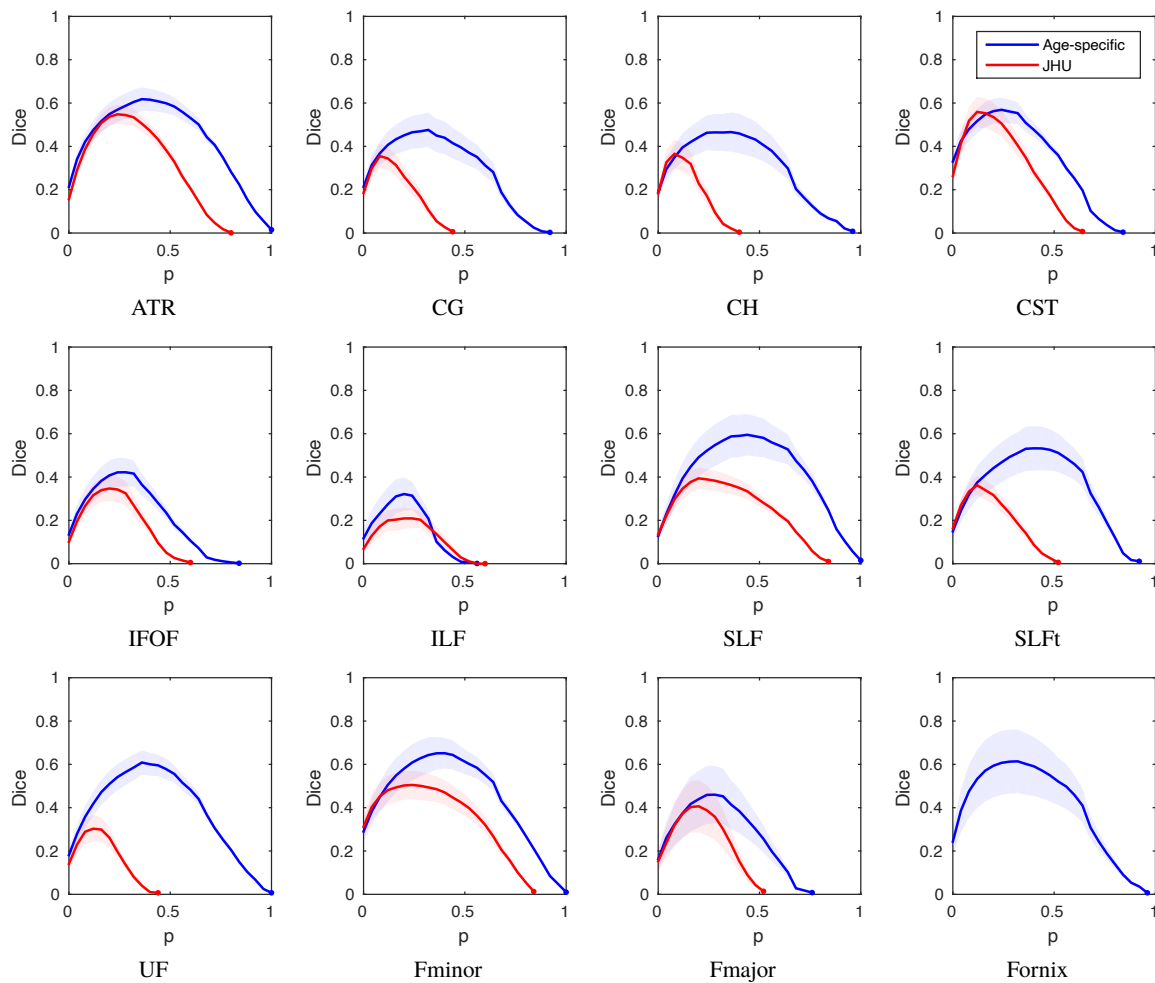

Figure 5: Same-site validation of tract overlap with "gold-standard" subject specific tract tracing. Plots show the Dice score of volumetric overlap (y axis) against probability threshold (x axis) when using the age-specific atlas (blue) or the JHU adult atlas (red), plotted up to the threshold at which no voxels remain. Lines show the median score for the 8 validation subjects not included in the formation of the atlas, and shaded regions show the 95% confidence interval. Note that the age-specific atlas (derived from data acquired on the same scanner, but different subjects), outperformed

13

293   the JHU (adult) atlas in all tracts. The tract representing the fornix is not available in the JHU atlas so

294   only the new mask was tested.

295   **3.3.2 DWI Metrics**

296   The correlation between FA in slices measured by the age-specific atlas and individual tracing is

297   shown for the same-site validation data in Figure 6, with correlation coefficients given in Table S1

298   and Figure S2. The correlation for the ABIDE data is shown in Figure S3, with coefficients given in

299   Table S2 and Figure S4. Better agreement between the "gold-standard" (i.e. individual tract tracing)

300   and the FA estimated from the different atlases (age-specific or JHU) is reflected by slopes closer to

301   one, and smaller spread of data around this line. In the same-site data, most tracts show strong

302   correlation between FA measured by the age-specific atlas and that measured by tracing in the

303   individual, with all tracts having $r > 0.8$ apart from the CG ($r = 0.60$), SLF ($r = 0.50$) and SLFt ($r =$

304   0.54). In the ABIDE data, seven of the twelve tracts have $r > 0.7$, with the exception of the CG ($r =$

305   0.67), CH ($r = 0.62$), SLF ($r = 0.66$), SLFt ($r = 0.51$) and UF ($r = 0.69$). The age-specific atlas almost

306   always performs better than the JHU atlas; in the same-site validation, every tract exhibits higher

307   correlation when delineated with the age-specific atlas than with the JHU atlas, and in the ABIDE

308   data this is the case for all tracts apart from the SLF (age-specific $r = 0.66$; JHU $r = 0.70$), the IFOF

309   (for which both atlases give the same correlation, $r = 0.88$) and the CST (for which both atlases give

310   the same correlation, $r = 0.89$).

311
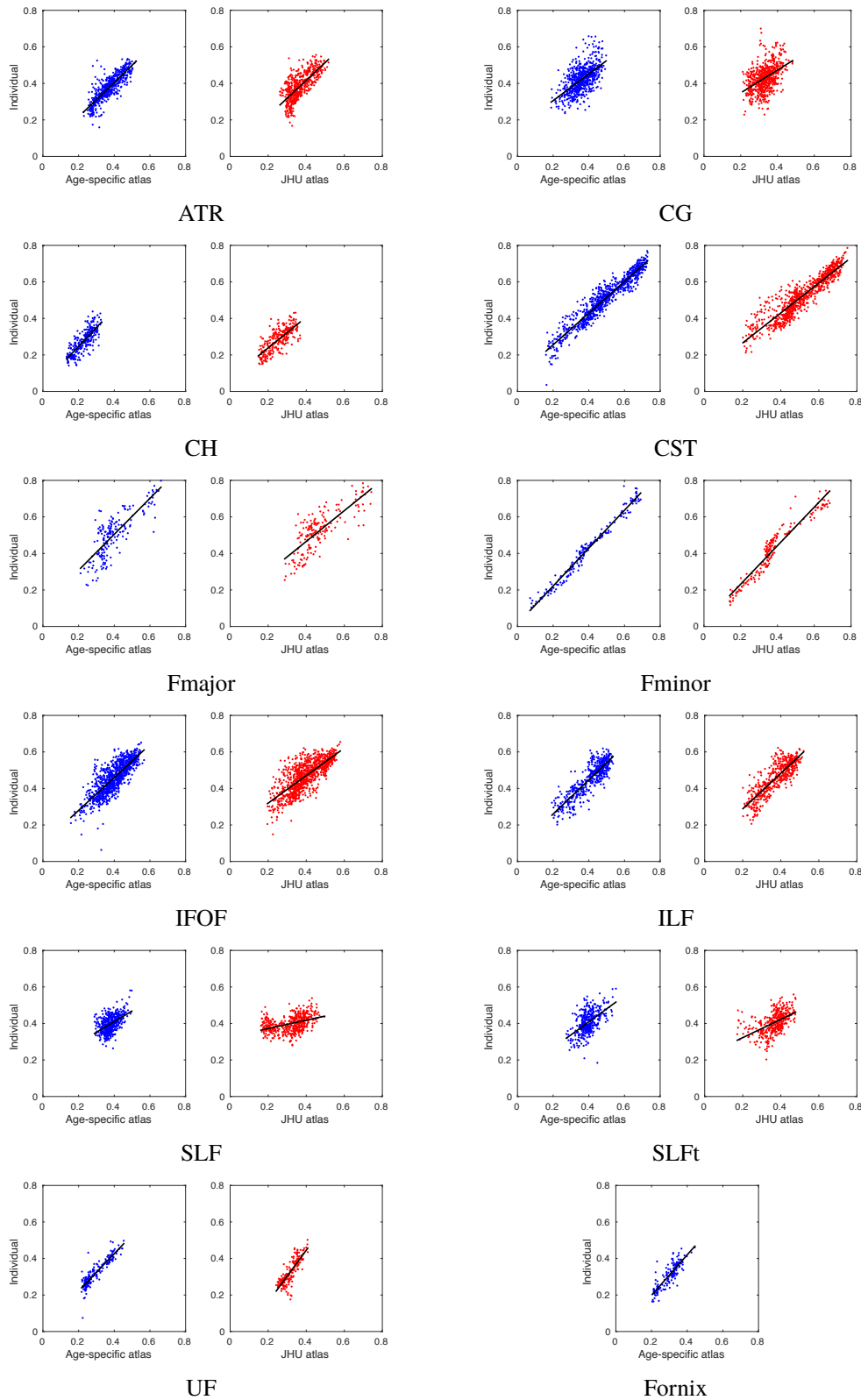
Figure 6: Same-site validation of slice FA values. Plots show slice FA measured from individually traced tracts (i.e. the "gold-standard") plotted against corresponding values extracted from the age-specific and JHU atlases. Each plot shows a point for every slice in each of the 8 validation subjects and the regression.

316   The whole-tract FA measured by the atlas is plotted against that given by tracing in individuals in

317   Figure 7 and Bland-Altman plots are shown in Figure 8. The fornix is not included in these plots to

318   allow valid comparison with the JHU atlas. For both the same-site and ABIDE validation data, the

319   regression to the age-specific atlas measurements has slope closer to unity and intercept closer to zero

320   than the JHU atlas (see Figure 7). The age-specific atlas also shows stronger correlation than the JHU

321   atlas for both same-site data (age-specific r = 0.72; JHU r = 0.54) and ABIDE data (age-specific r =

322   0.75; JHU r = 0.72). Both the age-specific atlas and the JHU atlas have a positive bias compared to

323   the individual measurements in the same-site and ABIDE data. Considering the Bland-Altman plots

324   (Figure 8), the age-specific atlas has narrower limits of agreement (LOA) than the JHU atlas in both

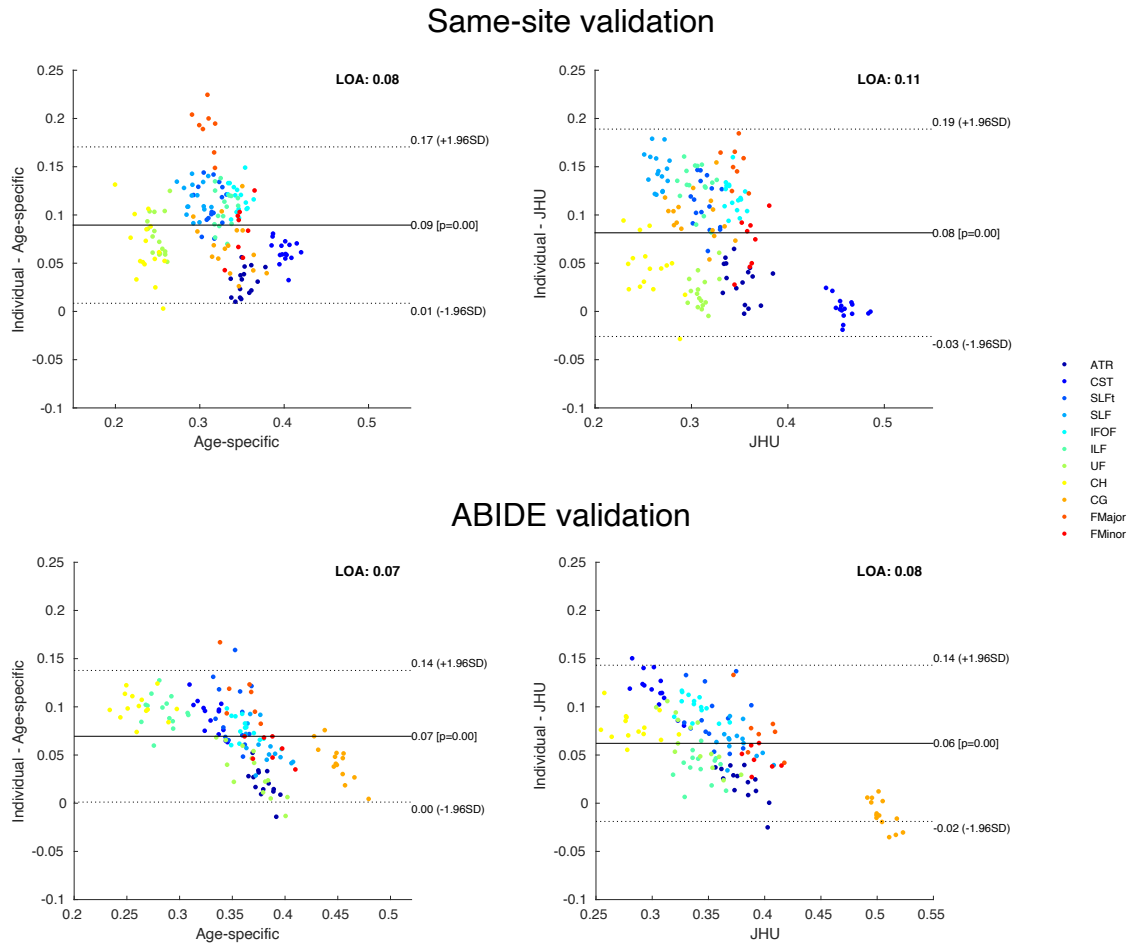325   the same-site and ABIDE data.
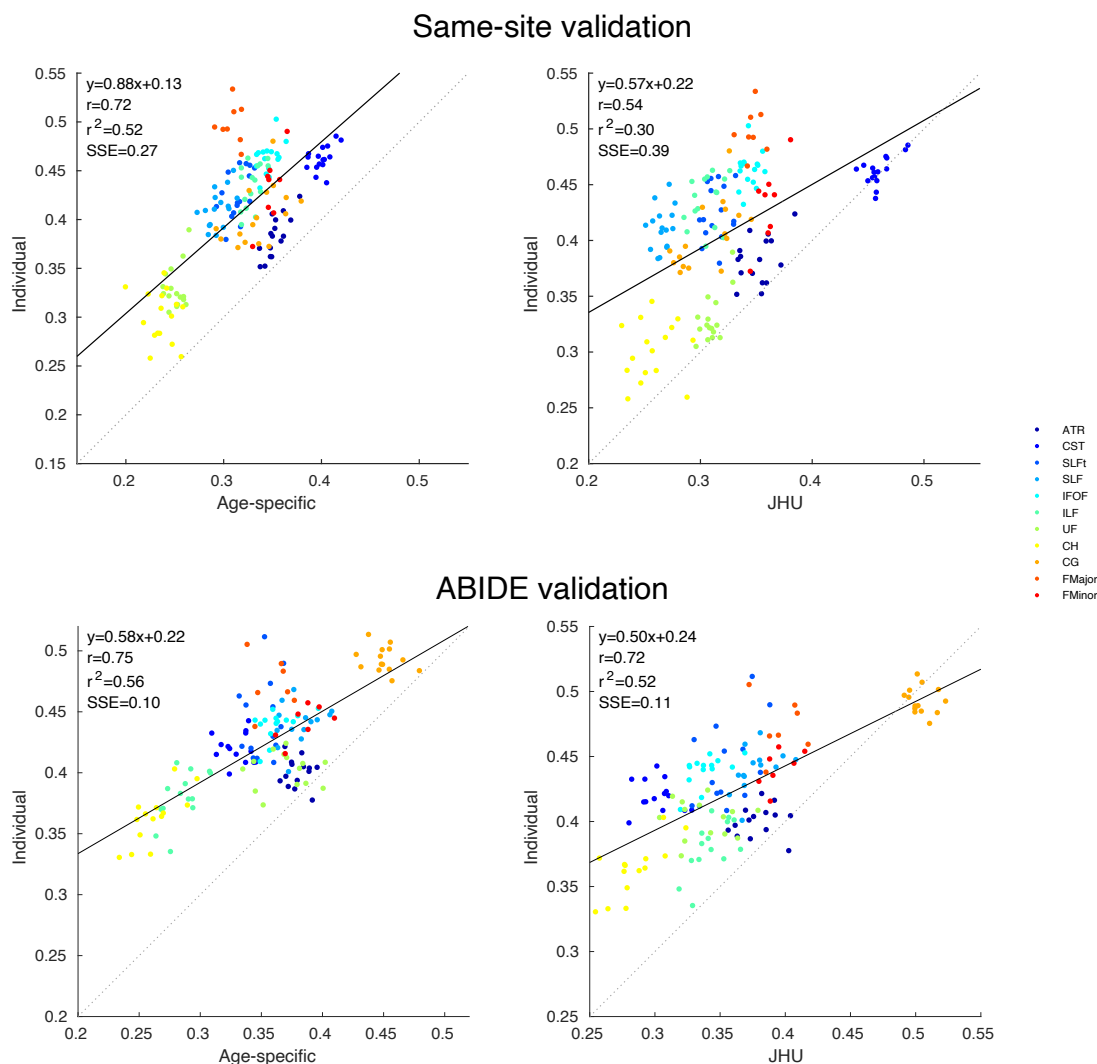
326

327   **Figure 7:** Comparison of mean FA extracted from whole tracts traced in individuals ("gold-

328   standard") and that estimated using the age-specific or JHU (adult) atlases. FA in individually traced

329   tracts is plotted against tract FA measured by the probabilistic atlases for same-site data (top row) and

330   ABIDE data (bottom row). The solid line shows the regression, and the dotted line represents exact

16

331 equality between individual and the age-specific or JHU data. Displayed on each plot is the slope and

332 intercept equation, the Pearson correlation coefficient, r, the squared Pearson correlation coefficient,

333 r^2, and the sum of squared error (SSE).

334

335 **Figure 8:** Bland-Altman plots for whole-tract average FA measurements in same-site data (top row)

336 and ABIDE data (bottom row), plotted for both the age-specific atlas (left) and JHU atlas (right). The

337 limits of agree

338 **3.4 Case Stu**

339 Numerous trac   controls (see Table

340 S3). After Bor   1), left SLF (p =

341 0.0383), and fo   to controls. Box

342 plots for these
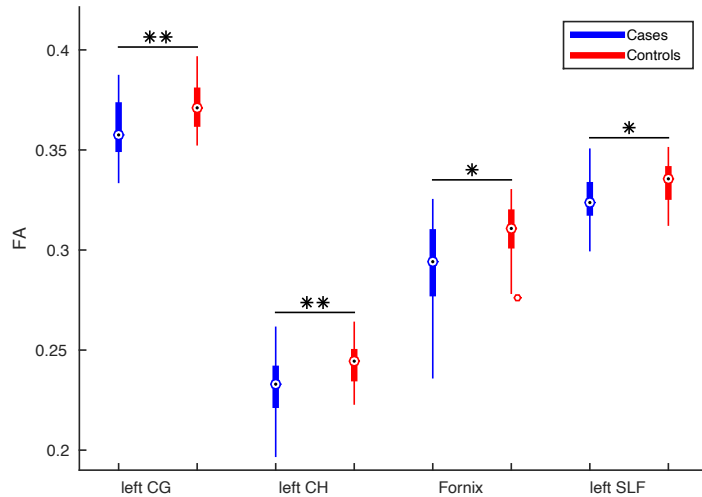
Figure 9: Box plots of significant differences in whole-tract average FA between children treated with TH for NE and healthy controls. *p < 0.05 **p<0.01, Bonferroni corrected.

The same analysis was run with the JHU atlas for comparison (see Table S4). Three tracts which were significant before Bonferroni correction when measured using the age-specific atlas, were not significant with the JHU atlas. Additionally, the left SLF, which was significant after correction when measured with the age-specific atlas, did not survive correction when measured with the JHU atlas. The left CG was significant with both atlases after correction; however, the p-value was lower when measured with the age-specific atlas. The left CH was significant after correction when measured with both atlases and was slightly more significant when measured with the JHU atlas. The right CH was significant after correction when measured with the JHU atlas but not the age-specific atlas. The fornix was significant when measured with the age-specific atlas but is not available in the JHU atlas so could not be tested.

4 Discussion

This study introduces an age-specific probabilistic white matter atlas constructed from children aged 6-8 years, providing a method of delineating white matter tracts in younger cohorts who may be averse to the long scanning times required for tractography based on HARDI data. We have shown that this atlas accurately delineates tracts in children from a same-site cohort aged 6-8 years, and a cohort from a different site, imaged with different scanner and acquisition protocol, aged 8-9 years. The strong correlation between FA sampled by the atlas and that measured in each individual (i.e. the "gold-standard"), at both a whole-tract level and slice-wise level, shows that the atlas provides an accurate estimate for the underlying white matter microstructure. Additionally, the high Dice scores between tracts in the age-specific atlas and those delineated by tractography in each validation

18

366   individual demonstrate a high level of volumetric overlap (indicating improved anatomical accuracy

367   of the age-specific atlas). In both measures of validation, the age-specific atlas almost always

368   performs better than simply registering to an existing adult white matter tract atlas, as is routinely

369   done in the literature. As proof of concept, we applied the age-specific atlas to the CoolMRI study,

370   revealing significantly reduced FA in several major white matter tracts in children treated with TH for

371   NE at birth compared to healthy controls.

372   The correlation of whole-tract FA measured by the atlas with that given by individual tracing offers

373   quantification of the performance of the atlas as a whole. In both the same-site validation data and the

374   ABIDE validation data, the age-specific atlas exhibits stronger correlation with the individual

375   measurements, with the slope of the regression closer to unity, than for the JHU atlas. The narrower

376   limits of agreement in the Bland-Altman plots and higher correlation coefficient for the age-specific

377   atlas indicate that this has higher precision than the JHU atlas. The strong correlation and high

378   precision of diffusion metrics sampled by the age-specific atlas shows that this can characterise the

379   distribution of tract-level diffusion metrics in a study group, facilitating more sensitive group

380   comparison and investigation of associations between these metrics and neuropsychological and

381   behavioural measures.

382   Those tracts which exhibit a lower correlation between atlas and individual slice-wise FA

383   measurements (namely the CG, SLF and SLFt, as well as the CH and UF in the ABIDE data) have

384   very little spread in FA values, resulting in tightly grouped measurements with a low correlation

385   coefficient, as shown in Figures 6 and S3. For these tracts, the Dice scores in Figures 5, as well as the

386   tract-wise validation in Figures 7 and 8 demonstrate improved performance of the age-specific atlas

387   on the level of whole tracts.

388   Long, thin tracts, such as the CST, IFOF and ILF, are particularly susceptible to partial volume effects

389   when measuring overlap; a small radial translation will result in a large change to the Dice score. In

390   these tracts, the high correlation in sampled FA values shows that the age-specific atlas gives accurate

391   measurement of the tract microstructure.

392   Multi-site validation alleviates bias associated with using the same scanner for validation data and

393   atlas construction. The age range of the ABIDE validation data is slightly higher than that of the atlas

394   data, simply due to data availability, however the age-specific atlas still performs better than that

395   obtained from adults i.e. the JHU atlas. Further bias may be introduced by the use of the same

396   tractography algorithm in atlas creation and the same-site validation data, thus a different tractography

397   algorithm was used for the ABIDE data, such that the results and conclusions drawn from them are

398   deliberately conservative. Whereas the FOD-based algorithm used to construct the age-specific atlas

399   uses spherical deconvolution to find the peak FOD in the closest orientation to the propagating

19

400   streamline, the tensor-based algorithm used for the ABIDE data propagates the streamline along the

401   principal eigenvector of the diffusion tensor at each step, similar to the tensor-based fibre tracking

402   algorithm used in the construction of the JHU atlas. Despite this bias towards the JHU atlas, the age-

403   specific atlas still performed better overall in the ABIDE validation.

404   This introduces the question of how to provide the "gold-standard" of fibre tracking; the tensor-based

405   algorithm was used for the ABIDE data in order to eliminate bias towards the age-specific atlas,

406   however this category of fibre tracking algorithm is widely acknowledged to give poor

407   characterisation of diffusion in brain white matter due to its inability to resolve crossing fibres

408   (Behrens et al., 2007; Tournier et al., 2012). Thus, the FOD-based algorithm used in the construction

409   of the atlas and in the same-site validation data, which facilitates more comprehensive tracing due to

410   its superior performance in regions of crossing fibres (Tournier et al., 2008), arguably gives a more

411   accurate representation of the ground truth (i.e. the underlying white matter fibres). Therefore, when

412   inspecting the volumetric overlap between the atlas and individually traced tracts in the validation

413   data, the same-site data traced with the FOD-based algorithm likely gives a better indication of

414   performance overall. Consequently, we believe the ABIDE validation provides a worst-case

415   performance estimate – the fibre tracking algorithm is comparable to the JHU atlas and the age range

416   is above that of the age-specific atlas – yet the age-specific atlas still out-performs the adult JHU atlas.

417   In future, as well as providing coverage of other age ranges, atlases could offer more extensive

418   labelling of additional tracts and regions of white matter. A comprehensive database of traced tracts

419   across a range of ages, potentially constructed by applying automated tractography-based white

420   matter tract segmentation protocols (Lawes et al., 2008; Verhoeven et al., 2009; Wassermann et al.,

421   2010; Zhang et al., 2018) to data from population studies such as the Human Connectome Project

422   (Van Essen et al., 2013), Developing Human Connectome Project (Hughes et al., 2017), or Baby

423   Connectome Project (Howell et al., 2019), would allow study-specific atlases to be built from subjects

424   matched to a given study cohort.

425   Applying the age-specific atlas to the CoolMRI study to investigate group differences in tract-level

426   FA revealed selective reduction in FA, that was significantly reduced in the left CG, left CH, left SLF

427   and the fornix. The differences in the left CG were more significant when measured with the age-

428   specific atlas than with the JHU atlas, and the differences in the left SLF are only significant with the

429   age-specific atlas. Additionally, several tracts which are significant before Bonferroni correction

430   when measured with the age-specific atlas are not significant with the JHU atlas. These results may

431   indicate improved sensitivity of the age-specific atlas facilitating more accurate measurements of the

432   distribution of FA values in each group. Differences in the right CH were significant when measured

433   with the JHU but not the age-specific atlas. The improved performance of the age-specific atlas in the

20

434   volumetric overlap and slice-wise correlation of the CH suggests that this may be a false positive

435   when measured with the JHU atlas. This comparison between the group differences revealed by each

436   atlas highlights the benefits of improved sensitivity when applying the atlas to a patient cohort.

437   However, it is important to recognise that in the absence of "ground truth" these comparisons are

438   qualitative in nature, and do not provide definitive evidence to support the use of one atlas over

439   another.

440   Previous studies of neonates treated with TH for NE have investigated the relationship between white

441   matter diffusion properties, measured in the first weeks following birth, and neurodevelopmental

442   outcome at 2 years of age. These studies found a significant reduction in FA in infants with adverse

443   outcomes, compared to those with favourable outcomes, in widespread areas of white matter

444   including, but not limited to the corpus callosum, anterior and posterior limbs of the internal capsule,

445   external capsule, fornix, cingulum, and ILF (Lally et al., 2019; Tusor et al., 2012). Many of these

446   regions were also shown to have reduced FA in the CoolMRI cases, indicating that the early structural

447   alterations resulting from the brain injury cause lasting changes to white matter development. These

448   results also provide evidence for an underlying white matter deficit which manifests as

449   neuropsychological differences seen at school-age (Jary et al., 2019; Lee-Kelland et al., 2020; Tonks

450   et al., 2019). Further investigation is required to link these structural impairments to specific

451   components of the cognitive and motor assessments, and to develop possible therapeutic intervention

452   strategies.

5 Conclusions

453

454   The age-specific atlas provided by this study has been shown to robustly delineate white matter tracts

455   in children aged 6-8 years. Diffusion metrics sampled by the atlas correlate strongly with those

456   measured by individual fibre tracking, allowing reliable investigation of white matter microstructure

457   in cohorts where running tractography in every individual may not be an option.

Acknowledgements

458

Funding

462

References

470   Altaye, M., Holland, S.K., Wilke, M., Gaser, C., 2008. Infant brain probability templates for MRI segmentation and
471   normalization. Neuroimage 43, 721–730. https://doi.org/10.1016/J.NEUROIMAGE.2008.07.060

472   Altman, D.G., Bland, J.M., 1983. Measurement in Medicine: The Analysis of Method Comparison Studies. Stat. 32, 307.
473   https://doi.org/10.2307/2987937

474   Ameis, S.H., Catani, M., 2015. Altered white matter connectivity as a neural substrate for social impairment in Autism
475   Spectrum Disorder. Cortex 62, 158–181. https://doi.org/10.1016/j.cortex.2014.10.014

476   Andersson, J.L.R., Jenkinson, M., Smith, S., 2007. Non-linear registration aka spatial normalisation [WWW Document].
477   FMRIB Tech. Rep. TRO7JA2. URL http://fmrib.medsci.ox.ac.uk/analysis/techrep/tr07ja2/tr07ja2.pdf

478   Andersson, J.L.R., Skare, S., Ashburner, J., 2003. How to correct susceptibility distortions in spin-echo echo-planar images:
479   application to diffusion tensor imaging. Neuroimage 20, 870–888. https://doi.org/10.1016/S1053-8119(03)00336-7

480   Andersson, J.L.R., Sotiropoulos, S.N., 2016. An integrated approach to correction for off-resonance effects and subject
481   movement in diffusion MR imaging. Neuroimage 125, 1063–1078.
482   https://doi.org/10.1016/J.NEUROIMAGE.2015.10.019

483   Arrigoni, F., Peruzzo, D., Gagliardi, C., Maghini, C., Colombo, P., Iammarrone, F.S., Pierpaoli, C., Triulzi, F., Turconi,
484   A.C., 2016. Whole-Brain DTI Assessment of White Matter Damage in Children with Bilateral Cerebral Palsy:
485   Evidence of Involvement beyond the Primary Target of the Anoxic Insult. Am. J. Neuroradiol. 37, 1347–1353.
486   https://doi.org/10.3174/ajnr.A4717

487   Asato, M.R., Terwilliger, R., Woo, J., Luna, B., 2010. White matter development in adolescence: A DTI study. Cereb.
488   Cortex 20, 2122–2131. https://doi.org/10.1093/cercor/bhp282

489   Assaf, Y., Johansen-Berg, H., Thiebaut de Schotten, M., 2019. The role of diffusion MRI in neuroscience. NMR Biomed.
490   32, e3762. https://doi.org/10.1002/nbm.3762

491   Assaf, Y., Pasternak, O., 2008. Diffusion Tensor Imaging (DTI)-based White Matter Mapping in Brain Research: A Review.
492   J. Mol. Neurosci. 34, 51–61. https://doi.org/10.1007/s12031-007-0029-0

493   Basser, P.J., Pajevic, S., Pierpaoli, C., Duda, J., Aldroubi, A., 2000. In vivo fiber tractography using DT-MRI data. Magn.
494   Reson. Med. 44, 625–632. https://doi.org/10.1002/1522-2594(200010)44:4<625::AID-MRM17>3.0.CO;2-O

495   Bastiani, M., Andersson, J.L.R., Cordero-Grande, L., Murgasova, M., Hutter, J., Price, A.N., Makropoulos, A., Fitzgibbon,
496   S.P., Hughes, E., Rueckert, D., Victor, S., Rutherford, M., Edwards, A.D., Smith, S.M., Tournier, J.-D., Hajnal, J. V.,
497   Jbabdi, S., Sotiropoulos, S.N., 2019. Automated processing pipeline for neonatal diffusion MRI in the developing
498   Human Connectome Project. Neuroimage 185, 750–763. https://doi.org/10.1016/J.NEUROIMAGE.2018.05.064

499   Behrens, T.E.J., Berg, H.J., Jbabdi, S., Rushworth, M.F.S., Woolrich, M.W., 2007. Probabilistic diffusion tractography with
500   multiple fibre orientations: What can we gain? Neuroimage 34, 144–155.
501   https://doi.org/10.1016/J.NEUROIMAGE.2006.09.018

502   Cascio, C.J., Gerig, G., Piven, J., 2007. Diffusion tensor imaging: Application to the study of the developing brain. J. Am.
503   Acad. Child Adolesc. Psychiatry 46, 213–223. https://doi.org/10.1097/01.chi.0000246064.93200.e8

504   Dennis, E.L., Thompson, P.M., 2013. Typical and atypical brain development: a review of neuroimaging studies. Dialogues
505   Clin. Neurosci. 15, 359–84.

506   Di Martino, A., O'Connor, D., Chen, B., Alaerts, K., Anderson, J.S., Assaf, M., Balsters, J.H., Baxter, L., Beggiato, A.,
507   Bernaerts, S., Blanken, L.M.E., Bookheimer, S.Y., Braden, B.B., Byrge, L., Castellanos, F.X., Dapretto, M., Delorme,
508   R., Fair, D.A., Fishman, I., Fitzgerald, J., Gallagher, L., Keehn, R.J.J., Kennedy, D.P., Lainhart, J.E., Luna, B.,
509   Mostofsky, S.H., Müller, R.-A., Nebel, M.B., Nigg, J.T., O'Hearn, K., Solomon, M., Toro, R., Vaidya, C.J.,
510   Wenderoth, N., White, T., Craddock, R.C., Lord, C., Leventhal, B., Milham, M.P., 2017. Enhancing studies of the
511   connectome in autism using the autism brain imaging data exchange II. Sci. Data 4, 170010.
512   https://doi.org/10.1038/sdata.2017.10

513   Dice, L.R., 1945. Measures of the Amount of Ecologic Association Between Species. Ecology 26, 297–302.
514   https://doi.org/10.2307/1932409

515   Dimond, D., Schuetze, M., Smith, R.E., Dhollander, T., Cho, I., Vinette, S., Ten Eycke, K., Lebel, C., McCrimmon, A.,
516   Dewey, D., Connelly, A., Bray, S., 2019. Reduced White Matter Fiber Density in Autism Spectrum Disorder. Cereb.
517   Cortex 29, 1778–1788. https://doi.org/10.1093/cercor/bhy348

518   Fonov, V., Evans, A.C., Botteron, K., Almli, C.R., McKinstry, R.C., Collins, D.L., 2011. Unbiased average age-appropriate
519   atlases for pediatric studies. Neuroimage 54, 313–327. https://doi.org/10.1016/j.neuroimage.2010.07.033

520   Griswold, M.A., Jakob, P.M., Heidemann, R.M., Nittka, M., Jellus, V., Wang, J., Kiefer, B., Haase, A., 2002. Generalized
521   autocalibrating partially parallel acquisitions (GRAPPA). Magn. Reson. Med. 47, 1202–1210.
522   https://doi.org/10.1002/mrm.10171

523   Hagmann, P., Sporns, O., Madan, N., Cammoun, L., Pienaar, R., Wedeen, V.J., Meuli, R., Thiran, J.-P., Grant, P.E., 2010.
524   White matter maturation reshapes structural connectivity in the late developing human brain. Proc. Natl. Acad. Sci.
525   107, 19067–19072. https://doi.org/10.1073/pnas.1009073107

526   Horsfield, M.A., Jones, D.K., 2002. Applications of diffusion-weighted and diffusion tensor MRI to white matter diseases - a
527   review. NMR Biomed. 15, 570–577. https://doi.org/10.1002/nbm.787

528   Howell, B.R., Styner, M.A., Gao, W., Yap, P.-T., Wang, L., Baluyot, K., Yacoub, E., Chen, G., Potts, T., Salzwedel, A., Li,
529   G., Gilmore, J.H., Piven, J., Smith, J.K., Shen, D., Ugurbil, K., Zhu, H., Lin, W., Elison, J.T., 2019. The UNC/UMN
530   Baby Connectome Project (BCP): An overview of the study design and protocol development. Neuroimage 185, 891–
531   905. https://doi.org/10.1016/J.NEUROIMAGE.2018.03.049

532   Hua, K., Zhang, J., Wakana, S., Jiang, H., Li, X., Reich, D.S., Calabresi, P.A., Pekar, J.J., van Zijl, P.C.M., Mori, S., 2008.
533   Tract probability maps in stereotaxic spaces: Analyses of white matter anatomy and tract-specific quantification.
534   Neuroimage 39, 336–347. https://doi.org/10.1016/j.neuroimage.2007.07.053

535   Hughes, E.J., Winchman, T., Padormo, F., Teixeira, R., Wurie, J., Sharma, M., Fox, M., Hutter, J., Cordero-Grande, L.,
536   Price, A.N., Allsop, J., Bueno-Conde, J., Tusor, N., Arichi, T., Edwards, A.D., Rutherford, M.A., Counsell, S.J.,
537   Hajnal, J. V., 2017. A dedicated neonatal brain imaging system. Magn. Reson. Med. 78, 794–804.
538   https://doi.org/10.1002/mrm.26462

539   Hüppi, P.S., Dubois, J., 2006. Diffusion tensor imaging of brain development. Semin. Fetal Neonatal Med. 11, 489–497.
540   https://doi.org/10.1016/j.siny.2006.07.006

541   Jary, S., Lee-Kelland, R., Tonks, J., Cowan, F.M., Thoresen, M., Chakkarapani, E., 2019. Motor performance and cognitive
542   correlates in children cooled for neonatal encephalopathy without cerebral palsy at school age. Acta Paediatr. Int. J.

23

543   Paediatr. 108, 1773–1780. https://doi.org/10.1111/apa.14780

544   Jenkinson, M., Bannister, P., Brady, M., Smith, S., 2002. Improved Optimization for the Robust and Accurate Linear

545   Registration and Motion Correction of Brain Images. Neuroimage 17, 825–841.

546   https://doi.org/10.1006/NIMG.2002.1132

547   Konrad, K., Eickhoff, S.B., 2010. Is the ADHD brain wired differently? A review on structural and functional connectivity

548   in attention deficit hyperactivity disorder. Hum. Brain Mapp. 31, 904–916. https://doi.org/10.1002/hbm.21058

549   Lally, P.J., Montaldo, P., Oliveira, V., Soe, A., Swamy, R., Bassett, P., Mendoza, J., Atreja, G., Kariholu, U., Pattnayak, S.,

550   Sashikumar, P., Harizaj, H., Mitchell, M., Ganesh, V., Harigopal, Sundeep, Dixon, J., English, P., Clarke, P.,

551   Muthukumar, P., Satodia, P., Wayte, S., Abernethy, L.J., Yajamanyam, K., Bainbridge, A., Price, D., Huertas, A.,

552   Sharp, D.J., Kalra, V., Chawla, S., Shankaran, S., Thayyil, S., Lally, P.J., Montaldo, P., Oliveira, V., Soe, A., Swamy,

553   R., Bassett, P., Mendoza, J., Atreja, G., Kariholu, U., Pattnayak, S., Sashikumar, P., Harizaj, H., Mitchell, M., Ganesh,

554   V., Harigopal, Sundeep, Dixon, J., English, P., Clarke, P., Muthukumar, P., Satodia, P., Wayte, S., Abernethy, L.J.,

555   Yajamanyam, K., Bainbridge, A., Price, D., Huertas, A., Sharp, D.J., Kalra, V., Chawla, S., Shankaran, S., Thayyil,

556   S., 2019. Magnetic resonance spectroscopy assessment of brain injury after moderate hypothermia in neonatal

557   encephalopathy: a prospective multicentre cohort study. Lancet Neurol. 18, 35–45. https://doi.org/10.1016/S1474-

558   4422(18)30325-9

559   Lawes, I.N.C., Barrick, T.R., Murugam, V., Spierings, N., Evans, D.R., Song, M., Clark, C.A., 2008. Atlas-based

560   segmentation of white matter tracts of the human brain using diffusion tensor tractography and comparison with

561   classical dissection. Neuroimage 39, 62–79. https://doi.org/10.1016/J.NEUROIMAGE.2007.06.041

562   Lebel, C., Treit, S., Beaulieu, C., 2019. A review of diffusion MRI of typical white matter development from early

563   childhood to young adulthood. NMR Biomed. 32, e3778. https://doi.org/10.1002/nbm.3778

564   Lebel, C., Walker, L., Leemans, A., Phillips, L., Beaulieu, C., 2008. Microstructural maturation of the human brain from

565   childhood to adulthood. Neuroimage 40, 1044–1055. https://doi.org/10.1016/j.neuroimage.2007.12.053

566   Lee-Kelland, R., Jary, S., Tonks, J., Cowan, F.M., Thoresen, M., Chakkarapani, E., 2020. School-age outcomes of children

567   without cerebral palsy cooled for neonatal hypoxic–ischaemic encephalopathy in 2008–2010. Arch. Dis. Child. - Fetal

568   Neonatal Ed. 105, 8–13. https://doi.org/10.1136/archdischild-2018-316509

569   Moeller, S., Yacoub, E., Olman, C.A., Auerbach, E., Strupp, J., Harel, N., Uğurbil, K., 2010. Multiband multislice GE-EPI

570   at 7 tesla, with 16-fold acceleration using partial parallel imaging with application to high spatial and temporal whole-

571   brain fMRI. Magn. Reson. Med. 63, 1144–1153. https://doi.org/10.1002/mrm.22361

572   Phan, T.V., Smeets, D., Talcott, J.B., Vandermosten, M., 2018. Processing of structural neuroimaging data in young

573   children: Bridging the gap between current practice and state-of-the-art methods. Dev. Cogn. Neurosci. 33, 206–223.

574   https://doi.org/10.1016/j.dcn.2017.08.009

575   Richards, J.E., Sanchez, C., Phillips-Meek, M., Xie, W., 2016. A database of age-appropriate average MRI templates.

576   Neuroimage 124, 1254–1259. https://doi.org/10.1016/J.NEUROIMAGE.2015.04.055

577   Sanchez, C.E., Richards, J.E., Almli, C.R., 2012. Age-specific MRI templates for pediatric neuroimaging. Dev.

578   Neuropsychol. 37, 379–399. https://doi.org/10.1080/87565641.2012.688900

579   Setsompop, K., Cohen-Adad, J., Gagoski, B.A., Raij, T., Yendiki, A., Keil, B., Wedeen, V.J., Wald, L.L., 2012a. Improving

580   diffusion MRI using simultaneous multi-slice echo planar imaging. Neuroimage 63, 569–580.

581   https://doi.org/10.1016/j.neuroimage.2012.06.033

582   Setsompop, K., Gagoski, B.A., Polimeni, J.R., Witzel, T., Wedeen, V.J., Wald, L.L., 2012b. Blipped-controlled aliasing in

583   parallel imaging for simultaneous multislice echo planar imaging with reduced g-factor penalty. Magn. Reson. Med.

584   67, 1210–1224. https://doi.org/10.1002/mrm.23097

585   Simmonds, D.J., Hallquist, M.N., Asato, M., Luna, B., 2014. Developmental stages and sex differences of white matter and
586   behavioral development through adolescence: A longitudinal diffusion tensor imaging (DTI) study. Neuroimage 92,
587   356–368. https://doi.org/10.1016/J.NEUROIMAGE.2013.12.044

588   Smith, R.E., Tournier, J.-D., Calamante, F., Connelly, A., 2013. SIFT: Spherical-deconvolution informed filtering of
589   tractograms. Neuroimage 67, 298–312. https://doi.org/10.1016/j.neuroimage.2012.11.049

590   Smith, S.M., Jenkinson, M., Woolrich, M.W., Beckmann, C.F., Behrens, T.E.J., Johansen-Berg, H., Bannister, P.R., De
591   Luca, M., Drobnjak, I., Flitney, D.E., Niazy, R.K., Saunders, J., Vickers, J., Zhang, Y., De Stefano, N., Brady, J.M.,
592   Matthews, P.M., 2004. Advances in functional and structural MR image analysis and implementation as FSL.
593   Neuroimage 23, S208–S219. https://doi.org/10.1016/J.NEUROIMAGE.2004.07.051

594   Sydnor, V.J., Rivas-Grajales, A.M., Lyall, A.E., Zhang, F., Bouix, S., Karmacharya, S., Shenton, M.E., Westin, C.-F.,
595   Makris, N., Wassermann, D., O'Donnell, L.J., Kubicki, M., 2018. A comparison of three fiber tract delineation
596   methods and their impact on white matter analysis. Neuroimage 178, 318–331.
597   https://doi.org/10.1016/j.neuroimage.2018.05.044

598   Tonks, J., Cloke, G., Lee-Kelland, R., Jary, S., Thoresen, M., Cowan, F.M., Chakkarapani, E., 2019. Attention and visuo-
599   spatial function in children without cerebral palsy who were cooled for neonatal encephalopathy: a case-control study.
600   Brain Inj. 33, 894–898. https://doi.org/10.1080/02699052.2019.1597163

601   Tournier, J.-D., Calamante, F., Connelly, A., 2013. Determination of the appropriate b value and number of gradient
602   directions for high-angular-resolution diffusion-weighted imaging. NMR Biomed. 26, 1775–1786.
603   https://doi.org/10.1002/nbm.3017

604   Tournier, J.-D., Calamante, F., Connelly, A., 2012. MRtrix: Diffusion tractography in crossing fiber regions. Int. J. Imaging
605   Syst. Technol. 22, 53–66. https://doi.org/10.1002/ima.22005

606   Tournier, J.-D., Calamante, F., Connelly, A., 2007. Robust determination of the fibre orientation distribution in diffusion
607   MRI: Non-negativity constrained super-resolved spherical deconvolution. Neuroimage 35, 1459–1472.
608   https://doi.org/10.1016/j.neuroimage.2007.02.016

609   Tournier, J.-D., Smith, R., Raffelt, D., Tabbara, R., Dhollander, T., Pietsch, M., Christiaens, D., Jeurissen, B., Yeh, C.-H.,
610   Connelly, A., 2019. MRtrix3: A fast, flexible and open software framework for medical image processing and
611   visualisation. Neuroimage 202, 116137. https://doi.org/10.1016/j.neuroimage.2019.116137

612   Tournier, J.-D., Yeh, C.-H., Calamante, F., Cho, K.-H., Connelly, A., Lin, C.-P., 2008. Resolving crossing fibres using
613   constrained spherical deconvolution: Validation using diffusion-weighted imaging phantom data. Neuroimage 42,
614   617–625. https://doi.org/10.1016/J.NEUROIMAGE.2008.05.002

615   Tusor, N., Wusthoff, C., Smee, N., Merchant, N., Arichi, T., Allsop, J.M., Cowan, F.M., Azzopardi, D., Edwards, A.D.,
616   Counsell, S.J., 2012. Prediction of neurodevelopmental outcome after hypoxic–ischemic encephalopathy treated with
617   hypothermia by diffusion tensor imaging analyzed using tract-based spatial statistics. Pediatr. Res. 72, 63–69.
618   https://doi.org/10.1038/pr.2012.40

619   Van Essen, D.C., Smith, S.M., Barch, D.M., Behrens, T.E.J., Yacoub, E., Ugurbil, K., 2013. The WU-Minn Human
620   Connectome Project: An overview. Neuroimage 80, 62–79. https://doi.org/10.1016/J.NEUROIMAGE.2013.05.041

621   Verhoeven, J.S., Sage, C.A., Leemans, A., Van Hecke, W., Callaert, D., Peeters, R., De Cock, P., Lagae, L., Sunaert, S.,
622   2009. Construction of a stereotaxic DTI atlas with full diffusion tensor information for studying white matter
623   maturation from childhood to adolescence using tractography-based segmentations. Hum. Brain Mapp. NA-NA.
624   https://doi.org/10.1002/hbm.20880

625 Wakana, S., Caprihan, A., Panzenboeck, M.M., Fallon, J.H., Perry, M., Gollub, R.L., Hua, K., Zhang, J., Jiang, H., Dubey,
626   P., Blitz, A., van Zijl, P., Mori, S., 2007. Reproducibility of quantitative tractography methods applied to cerebral
627   white matter. Neuroimage 36, 630–644. https://doi.org/10.1016/j.neuroimage.2007.02.049

628 Wassermann, D., Bloy, L., Kanterakis, E., Verma, R., Deriche, R., 2010. Unsupervised white matter fiber clustering and
629   tract probability map generation: Applications of a Gaussian process framework for white matter fibers. Neuroimage
630   51, 228–241. https://doi.org/10.1016/J.NEUROIMAGE.2010.01.004

631 Zhang, F., Wu, Y., Norton, I., Rigolo, L., Rathi, Y., Makris, N., O'Donnell, L.J., 2018. An anatomically curated fiber
632   clustering white matter atlas for consistent white matter tract parcellation across the lifespan. Neuroimage 179, 429–
633   447. https://doi.org/10.1016/J.NEUROIMAGE.2018.06.027

634